

# Infrared Camera Using a Single Nano-Photodetector

Hongzhi Chen, *Student Member, IEEE*, Ning Xi, *Fellow, IEEE*, Bo Song, *Student Member, IEEE*,  
Liangliang Chen, Jianguo Zhao, *Student Member, IEEE*, King Wai Chiu Lai, *Member, IEEE*,  
and Ruiguo Yang, *Student Member, IEEE*

**Abstract**—Infrared (IR) cameras have versatile applications; however, the low performance and high cost of conventional photodetectors have prevented their widespread utilization in various fields. Nano-materials have recently emerged as possible sensing elements of nano-photodetectors, and have exhibited data that may outperform their conventional counterparts. Carbon nanotube (CNT), a promising nano-material with excellent optical properties, has been employed to develop high performance photodetectors with low noise, tunable bandgap, and noncryogenic cooled operation. However, it is difficult to fabricate a large scale CNT photodetector array that can be integrated into traditional IR camera structures. In order to take advantage of the outstanding performance of the nano-photodetectors and overcome the fabrication difficulties to achieve high resolution and efficient imaging, we present a compressive sensing-based IR camera using a single pixel CNT photodetector. A photonic cavity is developed to integrate with the CNT photodetector so as to increase the absorption area of the device. The camera system uses the CNT photodetector to compressively sample the linear projections of the images onto binary random patterns. Employing the compressive sensing algorithm, high resolution imaging can be achieved with many fewer samples than the original image dimension. The camera is demonstrated effectively in order to observe the dynamic movement of a laser spot. By adaptively adjusting the camera setup, a zooming technique is developed to image small features. To our knowledge, this is the first demonstration of an IR camera using a nano-size photodetector. Our work shows that compressive sensing-based cameras have the potential to complement or selectively replace conventional IR imaging systems.

**Index Terms**—Carbon nanotube, compressive sensing, infrared camera, nano-sensor, photodetector, photonic crystal.

## I. INTRODUCTION

**I**NFRARED cameras have found plenty of applications in a wide range of arenas, including homeland security, surveillance, target recognition, fire mapping, industrial inspection,

predictive maintenance, and so on [1]. The most important component of IR cameras is the photodetector, which mainly determines the performance of the cameras. There are two categories of conventional IR detectors: thermal detectors and photon detectors. Both have their own limitations: thermal detectors have slow response and low detectivity, while photon detectors have narrow spectral responsivity and are required to operate at cryogenic conditions, involving a bulky and expensive cooling system.

The poor performance of conventional photodetectors stems from utilizing planar materials as the sensing element. This inspired the exploration of nano-photodetectors by using nano-materials as the functional element. Nano-materials, including graphene [2], quantum dot [3], quantum well [4], nanowire [5], [6], nanobelt [7], and nanotube [8], have been used to develop high performance nano-photodetectors by taking advantage of their unique electrical and optical properties. In particular, carbon nanotubes (CNTs) possess extraordinary optoelectronic properties thanks to their seamless nano-cylinder structures, making them an ideal material for nano-photodetectors [9].

CNT is a one dimensional (1D)-material that allows the free transportation of carriers in one direction. 1D-materials possess a perfect geometry for photon detection. It was demonstrated that a photon can effectively generate multiple electron and hole pairs in a CNT, which could potentially increase the quantum efficiency and sensitivity of nano-photodetectors [10]. The phonon scattering in 1D-photodetectors (1D-materials based nano-photodetectors) was suppressed in the circumferential direction, resulting in lower dark current and noise [11]. The high surface-to-volume ratio of the 1D-materials can prolong photocarriers' life time and shorten their transit time, which can enhance the signal-to-noise ratio [12]. The spectral responsivity of 1D-photodetectors can be modulated by controlling the diameter of the 1D-materials, since the bandgap energies of quantum confined structures are inversely proportional to their diameters [13], [14]. CNT based photovoltaic IR detectors was demonstrated to effectively detect middle wave IR signals without cryogenic cooling [15]. With the ongoing exploration of their underlying physics and improvement of fabrication techniques, 1D-photodetectors could potentially outperform conventional photodetectors and ultimately become an important building block for IR imaging.

However, there are two major difficulties that hinder the integration of nano-photodetectors into a traditional IR camera. Firstly, it is difficult to fabricate a large scale nano-photodetector array due to the low efficiency and reliability of the current manufacturing techniques. We have reported a  $3 \times 3$

Manuscript received May 31, 2012; revised September 4, 2012; accepted September 29, 2012. Date of publication October 18, 2012; date of current version January 29, 2013. This work was supported in part by the National Science Foundation under Grant IIS 0713346, and the ONR under Grant N00014-07-1-0935 and Grant N00014-04-1-0799. The associate editor coordinating the review of this paper and approving it for publication was Dr. Anna G. Mignani.

H. Chen, N. Xi, B. Song, L. Chen, J. Zhao, and R. Yang are with the Department of Electrical and Computer Engineering, Michigan State University, East Lansing, MI 48824 USA (e-mail: chenhon5@msu.edu; xin@egr.msu.edu; songbo@msu.edu; chenlia5@msu.edu; zhangj15@msu.edu; yangruig@msu.edu).

K. W. C. Lai was with the Department of Electrical and Computer Engineering, Michigan State University, East Lansing, MI 48824 USA. He is now with the Department of Mechanical and Biomedical Engineering, City University of Hong Kong, Kowloon, Hong Kong (e-mail: kinglai@egr.msu.edu).

Color versions of one or more of the figures in this paper are available online at <http://ieeexplore.ieee.org>.

Digital Object Identifier 10.1109/JSEN.2012.2225424

array of CNT photodetectors [16], but such a small number of sensors was unable to capture clear IR images. A  $13 \times 20$  array of GdSe nanowire based nano-photodetectors was fabricated, whereas a number of dead pixels were produced and the photo-responses of the sensors were not uniform [17]. Compared to the focal plane array of conventional image sensors, manufacturing mega-pixel nano-photodetectors is technically and economically inefficient. Secondly, 1D-photodetectors have a small absorption area due to the nano-size diameter of 1D-materials. Photodetectors using CNT thin film were reported to increase the absorption area [18]. However, the mixture of different CNTs and interaction between nanotubes severely degraded their photo-responses, thus photodetectors using an individual or parallel array of nanowires or nanotubes were desired. Although Z. Fan, etc. used parallel arrays of multiple nanowires as the sensing element, the fill factor (the ratio of sensing area to pixel size) of each pixel was still small [17].

In this paper, we will introduce a novel IR camera system, which enables utilizing the promising performance of 1D-photodetectors, and overcoming the difficulties to obtain high resolution and efficient IR images. The camera system is constructed based on an emerging compression theory: compressive sensing. A given image can be compressed if the image is sparse or can be sparsely represented in another basis, for example piecewise smooth images are sparse in wavelet basis. Traditional compression algorithms perform compression after sampling, while compressive sensing allows image compression during sampling so as to reduce the number of measurements and data storage capacity [19], [20].

Our camera system mainly consisted of a digital micromirror device (DMD), a CNT photodetector, a high speed readout system, and an image reconstruction computer. Instead of projecting IR images onto the focal plane array of image sensors, IR images were projected onto a DMD, which generates measurement matrices according to compressive sensing algorithms [21]. The images are compressively sampled using a single CNT photodetector via recording the linear projection of IR images onto the measurement matrix. IR images are recovered through a compressive sensing reconstruction algorithm based on the measurement results.

Experimental results showed that an IR image with 2500 pixels can be recovered by only 800 measurements. The camera was able to observe the dynamic movement of a laser spot. We also investigated the geometry of the laser spot through a zooming technique. It should be noted that this is the first report of an IR camera employing a nano-size photodetector. This camera architecture provides a novel platform to effectively capture high resolution IR images by using a single CNT photodetector. This imaging system may accelerate the development of IR cameras that utilize other high performance nano-photodetectors.

## II. COMPRESSIVE SENSING THEORY

The core of our IR camera system is compressive sensing theory. In this section, the basics of compressive sensing will be briefly reviewed. A recent complete introduction of this topic can be found in [22]. Compressive sensing is a

new paradigm for signal sampling, which has found a wide spectrum of applications in imaging [23], control and robotics [24], [25], geophysical data analysis [26], communication [27], and etc. Traditional sampling approaches require the sampling rate to be at least twice the maximum frequency of the signals according to the Nyquist-Shannon sampling theorem. Nevertheless, compressive sensing shows that the sampling rate can be significantly reduced if the signal satisfies general sparse conditions. Specifically, this new sensing paradigm directly samples the signal in compressed form, and then recovers the original signals by advanced optimization or greedy algorithms [28].

The general compressive sensing theory can be summarized as follows. Assume an unknown high dimensional signal  $x \in \mathbb{R}^n$  is projected to lower dimensional measurements  $y \in \mathbb{R}^m$ :

$$y = \Phi x \quad (1)$$

with  $\Phi \in \mathbb{R}^{m \times n}$  ( $m < n$ ) being the measurement matrix. Then the unknown  $x$  can be recovered from  $y$ , if  $x$  and  $\Phi$  satisfy certain conditions. In what follows, the conditions of both  $x$  and  $\Phi$  for successful recovery will be briefly described.

One condition for recovery is that the original signal is sparse (or approximately sparse) or has a sparse representation in some basis. A vector  $x \in \mathbb{R}^n$  is  $S$ -sparse if the support, i.e., the number of nonzero elements, of  $x$  is at most  $S$ . Denote the set of all the  $S$ -sparse vectors by  $\Omega_S$ . Formally,

$$\Omega_S = \{x \in \mathbb{R}^n : \|x\|_0 \leq S\}$$

where  $\|x\|_0$  denotes the support of  $x$ .

In some cases,  $x \in \mathbb{R}^n$  may not be sparse in its original form but sparse in some orthonormal basis. Let  $\Psi$  be such a basis. In this case,  $x$  can be expanded in  $\Psi$  as:  $x = \Psi \tilde{x}$  with  $\tilde{x} \in \Omega_S$ . The compressive sensing can be rewritten as:

$$y = \Phi x = A \tilde{x} \quad (2)$$

with  $A = \Phi \Psi$  being the new measurement matrix. Without loss of generality, we will assume the original signal is sparse (or approximately sparse) and use  $x$  to represent it in the following discussion.

In general, the exact  $S$ -sparse cannot be achieved in real-world signals, but they can be well approximated by an  $S$ -sparse signal. The best  $S$ -sparse approximation for a vector  $x \in \mathbb{R}^n$  is a vector  $x_S \in \mathbb{R}^n$  by retaining the largest  $S$  elements in  $x$  and setting the other elements to zero.

Another condition for recovery is that the measurement matrix needs to satisfy the restricted isometry property (RIP), which is defined as follows.

**Definition 1:** A matrix  $A \in \mathbb{R}^{m \times n}$  with  $m < n$  satisfies the RIP of order  $S$  if there exists a constant  $\sigma_S \in (0, 1)$  such that for any  $x \in \Omega_S$ , we have

$$(1 - \sigma_S) \|x\|_2^2 \leq \|Ax\|_2^2 \leq (1 + \sigma_S) \|x\|_2^2 \quad (3)$$

Note that measurement matrix can follow other conditions, such as spark [29], null space property [30], or coherence [29], but the RIP is the most powerful one because it can deal with the case when the measurements are corrupted by noise.

With the above two conditions, we can discuss the original signal recovery. To find the sparsest solution, the recovery problem can be stated as:

$$\min \|\hat{x}\|_0 \quad \text{subject to} \quad A\hat{x} = y \quad (4)$$

$\hat{x}$  is the recovered signal. The above problem, however, is NP-hard. As an alternative, the  $l_1$  minimization can be used:

$$\min \|\hat{x}\|_1 \quad \text{subject to} \quad A\hat{x} = y. \quad (5)$$

Using the  $l_1$  minimization, the recoverability is guaranteed by the following theorem.

**Theorem 1 (Candès [31]):** Suppose the matrix  $A$  satisfies the RIP of order  $2S$  with constant  $\sigma_{2S} < \sqrt{2} - 1$ , then the solution to Eq. (5) satisfies:

$$\|\hat{x} - x\|_2 \leq C\|x - x_S\|_1/\sqrt{S} \quad (6)$$

with  $C$  a constant related to  $\sigma_{2S}$ .

The theorem suggests that the error between the recovered signal and the original signal is bounded by the error between the original signal and the best  $S$ -sparse approximation. Note that the noise measurement can also be handled under the RIP condition [32], which will not be discussed here.

With the above theorem for recoverability, the next question is how to design the measurement matrix satisfying the RIP condition. The goal is to recover the original signal with the least measurements. In other words, we need to design the measurement matrix  $A \in \mathbb{R}^{m \times n}$  such that  $m$  is smallest for fixed  $n$ . Although it was difficult to design deterministic matrix for RIP, various random matrices were shown to satisfy the RIP with high probability. If the entries in the matrices are chosen according to Gaussian [33], Bernoulli [32], or sub Gaussian distribution [34], then the matrices satisfy the RIP with very high probability if:

$$m \geq D \cdot S \log(n/S) \quad (7)$$

where  $D$  is also a constant [34]. Note that the random matrices discussed above follows the so-called universality. In fact, if a random matrix  $\Phi$  satisfies the RIP, then the matrix  $\Phi\Psi$  will also satisfy the RIP with high probability. In other words, we can design the random measurement matrices  $\Phi$  without considering the sparsity of the original signal [32].

The final piece of compressive sensing is the recovery algorithm, i.e., the algorithm to solve Eq. (5). There are many algorithms to solve the problem, which can be classified into convex optimization, greedy algorithm, or combinatorial algorithms. A detailed summary of those algorithms can be found in [35].

### III. IR CAMERA SYSTEM

Our IR camera system, using a single pixel CNT photodetector, was constructed based on compressive sensing theory. The camera system structure will be introduced in this section, following the elucidation of its main components: CNT photodetector and DMD.

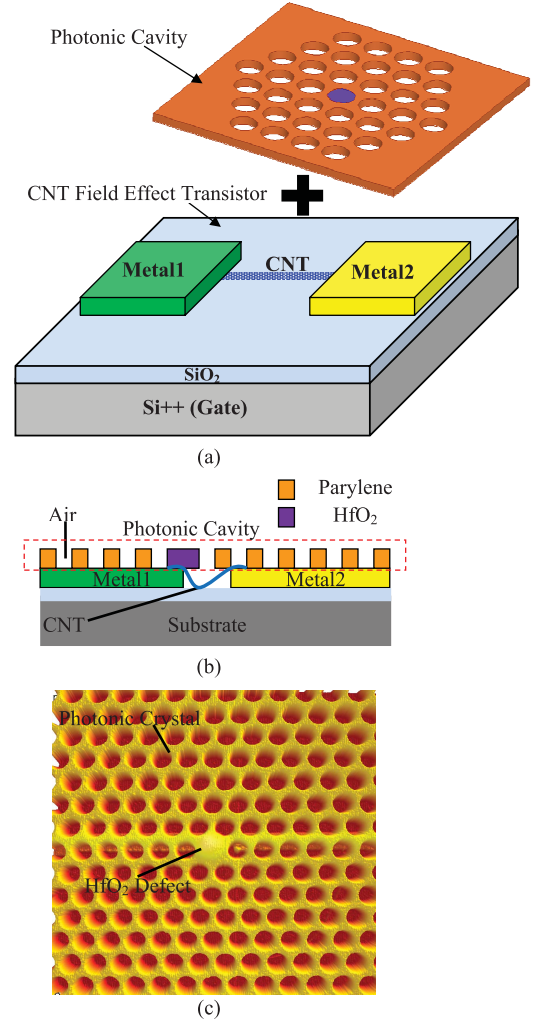


Fig. 1. (a) Basic structure of a CNT photodetector comprising a CNT field effect transistor and a photonic cavity. (b) Cross section of the device. (c) AFM image of a photonic cavity with an HfO<sub>2</sub> defect on top of a CNT field effect transistor.

#### A. CNT Photodetector

The main sensing component of our IR camera is a single pixel CNT photodetector. The CNT photodetector consists of two components: a CNT field effect transistor and a photonic cavity, as shown in Fig. 1(a). The CNT field effect transistor acts as the photo-sensor, converting photo-signals into electrical signals. The photonic cavity stacks on top of the transistor (Fig. 1(b)), serving as a light confinement element.

The CNT field effect transistor comprises an individual single wall CNT (SWCNT) connecting to high/low-workfunction metal electrodes, which serve as source and drain. The SWCNT, with diameter between 1 to 2 nm, was purchased from BuckyUSA, Inc. A heavily doped Si/SiO<sub>2</sub> substrate acts as a back gate of the transistor. The details of the working principle and fabrication technique were discussed in [36]. Briefly, when a CNT comes into contact with a metal, Schottky barrier may be formed depending on the Fermi energy alignment. Photocarriers will be separated by the built-in potential in the Schottky barriers [37], and thus photocurrent or photovoltage was produced for detection and quantification. The electrodes

were fabricated by ebeam lithography, thermal evaporation, and liftoff. CNT was deposited to bridge the electrodes using the dielectrophoresis (DEP) deposition system [38] and AFM manipulation system [39]. We have demonstrated that photodetectors using asymmetric metal structure with high/low-workfunctions have better performance than those with the same metals [40]. In our device, a metal structure of Au-CNT-Ti was adopted. Au and CNT form an ohmic or a quasi-ohmic contact, while Ti and CNT form a Schottky barrier. As a result, this asymmetric structure becomes a Schottky diode. The Si substrate acts as the gate for the photodetector, which can enhance the signal-to-noise ratio by simultaneously suppressing dark current and increasing photocurrent through electrostatic doping [41].

CNT field effect transistors showed promising performance in detecting IR signals, whereas nano-size diameters of CNTs limit their absorption area. Although optical antennas can enhance the photo-responses of CNT photodetectors [42], [43], they produce very limited increase in absorption area. For our CNT photodetector, a photonic cavity was utilized to enhance its absorption area. A photonic cavity is a photonic crystal embedded with a point defect, allowing light to concentrate into the defect [44]. By placing the photodetector onto the center of the defect, sensing area was extended from the CNT itself to the entire photonic cavity.

Photonic crystals are artificial optical materials with periodically structured dielectric materials of alternative reflective indices [45]. The propagation of light within photonic crystals can be manipulated by controlling the dimension of the dielectrics. The design of photonic crystals was stimulated by the periodic structure of solid state crystals. By constructing periodic structure with dimension in optical wavelengths range, photonic crystal can guide light with frequency bands and frequency bandgap in the same fashion as atomic lattices conducting electrons with energy bands and bandgap. If the optical frequency falls in frequency bands, a photonic crystal becomes a perfect optical conductor. On the other hand, when the photon frequency falls in a photonic bandgap, a photonic crystal acts like an optical insulator [46]. The photonic cavity was operated in the defect mode [47]: the point defect breaks the symmetric arrangement of the photonic crystal, and as a result, light (with a frequency in the photonic bandgap) propagating in the photonic crystal is trapped in the defect. Therefore, the photonic cavity can be considered as a micro-lens in our design.

Fig. 1(c) shows an AFM image of the photonic cavity fabricated on top of the CNT field effect transistor. The photonic cavity comprises a parylene slab with periodic air holes. An HfO<sub>2</sub> cylinder was used as the point defect, located on top of the transistor. The fabrication process was introduced in [48]. Traditional optical cavity is created by removing an air hole (point defect) in the photonic crystal, while an HfO<sub>2</sub> defect was utilized in our design. The refractive index of HfO<sub>2</sub> (1.90 [49]) is higher than parylene (1.62 [50]), which is higher than air (1.00). Therefore, total internal reflection will be more likely to occur between the HfO<sub>2</sub> and parylene, resulting in a higher percentage of light confinement in the defect region [48].

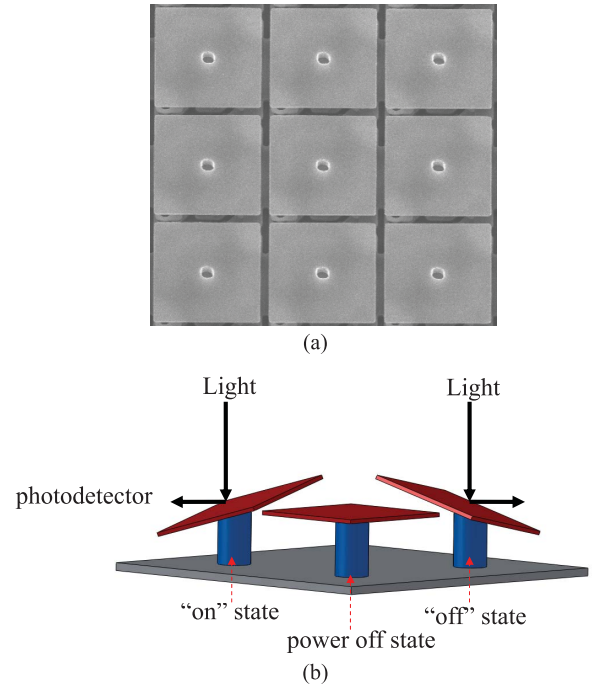


Fig. 2. (a) SEM image of nine micromirrors in a DMD. (b) Three statuses of the micro-mirrors: on, off, and power-off states.

### B. Digital Micromirror Device

DMD in our IR camera is one of the most important components to accomplish compressive sensing algorithm. Traditional DMD is the essential component of digital light processing (DLP) projection technology, controlling light propagation by a large array of electrostatically actuated micromirrors. Fig. 2(a) shows a scanning electron microscopy (SEM) image of nine micromirrors in a DMD. Each micromirror is square in shape, and stands closely to adjoining micromirrors with a small gap, implying a high fill factor. It should be noted that this camera system captures the images projected on the DMD, therefore it solves the low fill factor problem in the focal plane array of 1D-photodetectors [17].

In our imaging system, DMD from Texas Instruments (TI) was used to generate a measurement matrix according to compressive sensing. Each individual micromirror can be poised into two different angles ( $-10$  degree and  $+10$  degree), which define the "on" and "off" states of the micromirrors. In the "on" state, light irradiated on a micromirror is oriented to the CNT photodetector (the left mirror of Fig. 2(b)). In the "off" state, the light that fell onto a micromirror is reflected elsewhere (the right mirror of Fig. 2(b)). When the power for DMD is off, the micromirror stays horizontal without a rotation (the middle mirror of Fig. 2(b)). By controlling the states of each micromirror, the DMD forms a specific measurement matrix.

### C. Infrared Camera System

The structure of the IR camera system is built upon the compressive sensing theory introduced in the previous section. Fig. 3 depicts the system setup using a single pixel CNT photodetector as its image sensor. IR images were directed

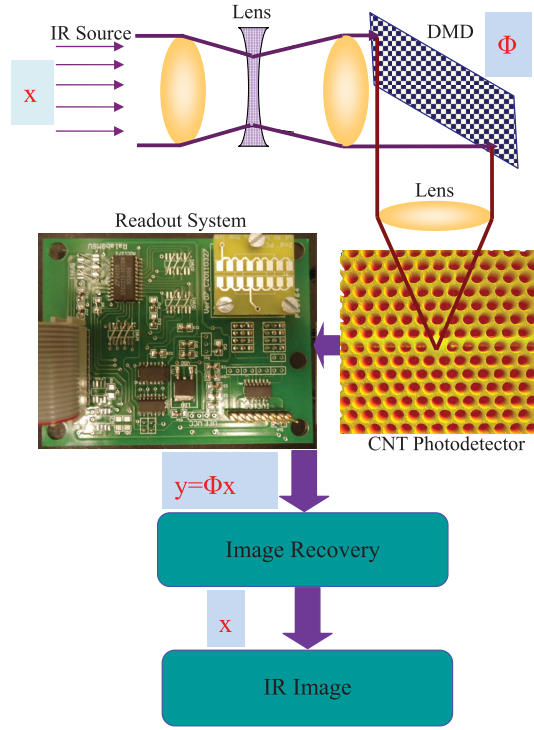


Fig. 3. Setup of the IR camera system using a CNT photodetector.

onto a DMD through a set of lenses. The IR images on the DMD represents the original signal  $x$  in Eq. (1) ( $x \in \mathbb{R}^n$ ,  $n$  is the number of image pixels). The DMD generated patterns according to a measurement matrix  $\Phi$  ( $\Phi \in \mathbb{R}^{m \times n}$ ) so as to compress the IR images. Each pattern on the DMD comprised  $n$  pixels, thus  $m$  different patterns were generated to construct the measurement matrix  $\Phi$ . The compressed IR images were reflected to another lens, which focused all the light to a CNT photodetector. The IR signal arrived at the CNT photodetector represents the linear projection of the images onto the measurement matrix, which can be considered as the inner product of IR images  $x$  and each row vector in the measurement matrix  $\Phi$ . The photocurrent generated in the photodetector was recorded by a fast readout system integrating with a charge integrator, an analog-to-digital converter (ADC), and a data acquisition (DAQ) card [51], [52]. The amplitudes of photocurrent represent the values of  $y$  in Eq. (1) ( $y \in \mathbb{R}^m$ ,  $m$  is the number of measurements). The IR images were recovered by a personal computer. It should be noted that compressive sensing makes  $m < n$ ; therefore, the IR images  $x$  were compressively sampled into the  $y$ . Based on the measurement results  $y$  and the designed measurement matrix  $\Phi$ , the original signal  $x$  can be recovered using an image reconstruction algorithm.

#### IV. EXPERIMENTAL RESULTS AND DISCUSSION

##### A. Photo-Responses

The CNT field effect transistor was fabricated and tested before being integrated to the IR camera. The electrical characteristics were measured with the Au electrode maintained at ground potential. The I-V characteristics at five different gate

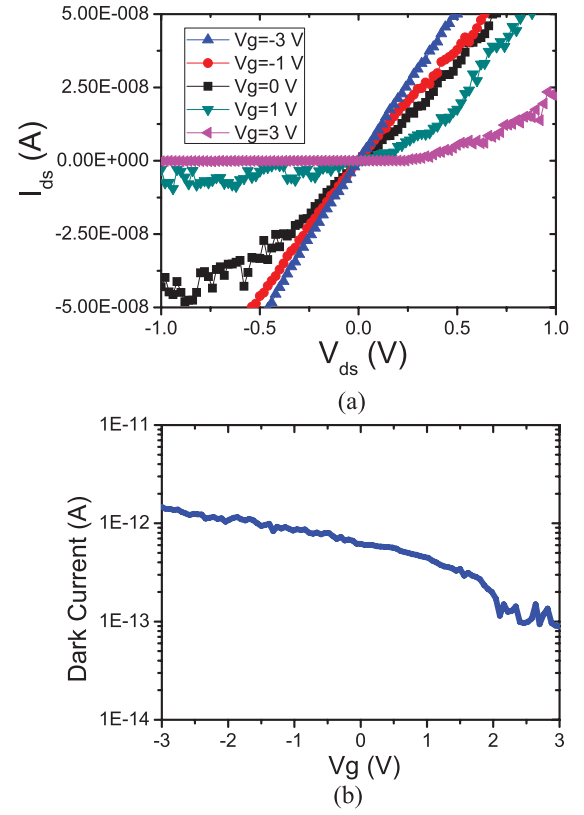


Fig. 4. (a) I-V characteristics of the CNT field effect transistor with five different gate voltages. (b) Transfer characteristics of the transistor at dark.

voltages ( $V_g$ ) are shown in Fig. 4(a) by sweeping the drain to source bias ( $V_{ds}$ ) from  $-1$  V to  $1$  V. A weak current rectifying was shown at zero gate voltage; a strong current rectifying was obtained at positive gate voltages, resulting in a typical diode electrical characteristic; while a linear I-V characteristic was observed at negative gate voltages. The reason is that gate voltages changed the Fermi energy of the CNT through electrostatic doping, which rearranged the energy alignment between CNT and metals, and hence altered the Schottky barriers [36].

Dark current was measured by sweeping the gate voltages from  $-3$  V to  $3$  V at zero drain to source bias, as illustrated in Fig. 4(b). Dark current was  $-6.1 \times 10^{-13}$  A at zero gate voltage. It was reduced to  $-9 \times 10^{-14}$  A at  $V_g = 3$  V. The dark current reduction at positive gate voltages resulted from the increase of Schottky barriers, which decreased thermally assist tunneling of carriers that is the dominant current injection in nanotubes [53]. A more detailed discussion can be found in [36]. It should be noted that the noise and dark current of the CNT field effect transistor were extremely low, with a magnitude of sub-picoampere.

The photo-responses of the device were measured by irradiating the sensing element with an IR laser that has 830 nm wavelength and a maximum power of 50 mW. A detailed introduction of the testing system was presented in [54]. In order to study the linearity and repeatability of the device, a triangular waveform control signal was applied to the laser. As a result, the output power of the laser was linearly ramped



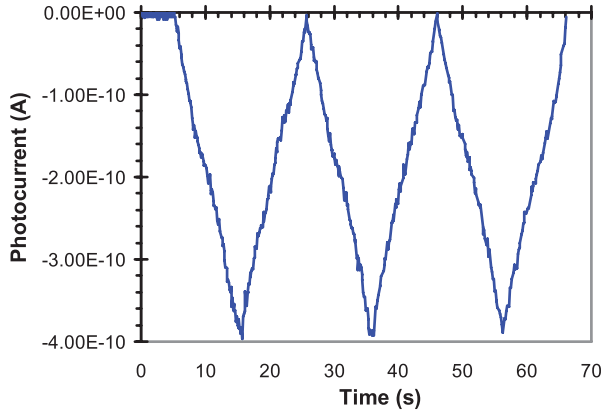


Fig. 5. Photo-responses of a CNT photodetector obtained by irradiating IR to the photodetector with the output power following a triangular waveform.

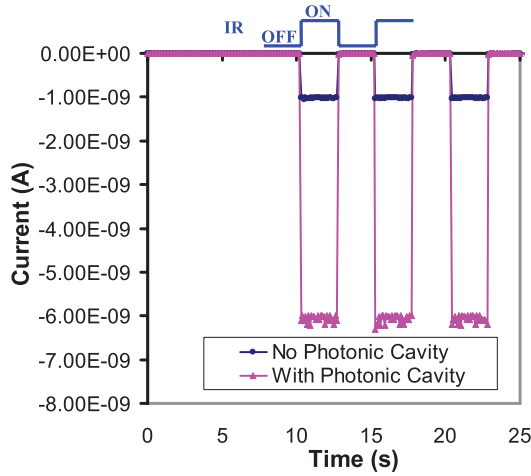


Fig. 6. Photo-responses of the CNT photodetector without and with the photonic cavity obtained by switching IR laser on and off at 0.2 Hz.

up and down between 0 to 50 mW. The device also exhibited a triangular form of photo-response, as shown in three cycles of photocurrent measurement in Fig. 5 (photocurrent is the current difference with presence and absence of IR irradiation). The photocurrent is linearly dependent on the output power with highest photocurrent of  $-3.95 \times 10^{-10}$  A at 50 mW laser power.

The photo-responses can be improved by applying a proper gate voltage to the back gate. The optimal gate voltage was found by recording the transfer characteristics of the transistor with absence and presence of IR irradiation [36]. With a gate voltage of 3 V, the photocurrent was boosted from  $-3.95 \times 10^{-10}$  A to  $-1 \times 10^{-9}$  A. It should be noted these results showed that positive gate voltages reduced dark current and enhanced photocurrent simultaneously due to the modulation of Schottky barriers [36].

Photonic cavity is an important component for our camera system, because it increases the effective absorption area of the photodetector. The blue curve in Fig. 6 shows the temporal photo-responses of the CNT photodetector without a photonic cavity by switching the IR laser on (50 mW) and off (0 W) periodically at 0.2 Hz with a gate voltage of 3 V. A photonic cavity was fabricated to integrate with

the photodetector with a dimension designed for concentrating light of 830 nm wavelength. After the fabrication of a  $30 \mu\text{m} \times 30 \mu\text{m}$  photonic cavity with an  $\text{HfO}_2$  defect on top of the CNT photodetector, the photocurrent collected by the CNT photodetector is increased to approximately  $-6 \times 10^{-9}$  A (Fig. 6), implying a 600% photocurrent enhancement via the photonic cavity.

### B. Stationary Infrared Images

By integrating this CNT photodetector into the camera system as shown in Fig. 3, we captured some stationary IR images as a performance test. The IR source is the same laser used for testing the stand free CNT photodetector.

For the imaging experiment, the laser source was projected onto the DMD to form an IR image  $x$ . DMD generated a measurement matrix  $\Phi$  according to random Bernoulli distribution, which had high probability of satisfying the RIP condition [32]. Each random pattern is a row of the measurement matrix, and  $m$  Bernoulli random patterns were used to capture an IR image. As a result, each measurement result from the CNT photodetector obtains the inner product between an IR image and a row of the measurement matrix. After  $m$  times of measurements, one image  $x$  is compressively sampled into the measurement results  $y$ . The image was recovered via minimizing the total variation norm (TV-norm). Minimizing such a norm can make the intensity difference between neighboring pixels sparse, thus smoothing the images. Formally, let  $x_{ij}$  be the pixel intensity in the  $i$ -th row and  $j$ -th column in the image  $x$ . The intensity differences in the horizontal and vertical directions ( $D_{ij}^h$  and  $D_{ij}^v$ ) can be defined respectively as follows:

$$D_{ij}^h = x_{i+1,j} - x_{ij}, \quad D_{ij}^v = x_{i,j+1} - x_{ij}. \quad (8)$$

The total variation for the image  $x$  is then defined as

$$TV(x) = \sum_{i,j} \sqrt{D_{ij}^h{}^2 + D_{ij}^v{}^2} \quad (9)$$

Therefore, the image recovery problem can be defined as:

$$\min ||TV(\hat{x})||_1 \quad \text{subject to} \quad A\hat{x} = y \quad (10)$$

Note that for consistence, the above  $\hat{x}$  can be considered as the vector form of the image matrix  $x$ .

The DMD has  $1064 \times 768$  micromirrors. Each micromirror is square in shape with a dimension of  $12 \mu\text{m} \times 12 \mu\text{m}$ . We first obtained IR images with a low resolution of  $30 \times 30$  pixels to adjust the alignment and focus of the system. Traditional cameras require 900 measurements in order to obtain a  $30 \times 30$  image, while our camera can recover the image with only 500 measurements [21]. Images of  $30 \times 30$  pixels correspond to  $1064 \times 768$  micromirrors, thus each pixel contains 908 micromirrors. Note that the DMD is not square in shape, thus each pixel in the image is a rectangular shape.

The IR camera was used to capture a higher resolution image of a rectangular IR light bar. The position, orientation, and geometry of the light bar on the DMD are shown in Fig. 7(a). The recovered image is shown in Fig. 7(b). The location and orientation of the recovered rectangular light bar,

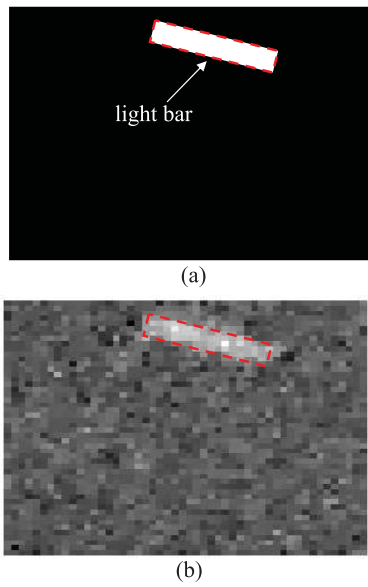


Fig. 7. (a) Position and orientation of the rectangular light bar on the DMD. (b) Image of  $50 \times 50$  pixels recovered by our IR camera, highlighted by a red rectangle.

highlighted by a red rectangle, are similar to that shown in Fig. 7(a). The image has a resolution of  $50 \times 50$  pixels. This image was recovered by only 800 measurements, which is less than 35% of the total pixel numbers (2500).

### C. Dynamic Observation

The IR camera was utilized to observe the dynamic movement of a laser spot. The laser spot was initially located at the lower left of the DMD, as shown in Fig. 8(a). We designed a trajectory of the laser spot movement: it was first moved downwards, and then moved upwards when the laser approached the bottom edge of the DMD. Six frames of the IR images captured by the camera were shown in Fig. 8. The resolution of these images is  $50 \times 50$  pixels, and 800 measurements were performed to recover the images using minimization TV-norm reconstruction algorithm. The images clearly show the movement of the laser spot following the designed path: the laser spot moved towards the bottom of the DMD in the first five frames (Fig. 8(a)–(e)), and it bounced upwards in the last frame (Fig. 8(f)).

However, it is difficult to identify the actual size and geometry of the laser spot from these images due to their low resolution. Fig. 8(b) shows the laser spot covered one pixel, while it covered three pixels in Fig. 8(c) and (e), and the rest of frames show the laser spot occupied two pixels. The spot size variation may be caused by the difference of the location of the laser spot: the laser spot covers one pixel if the spot resides at the center of a pixel, while it covers more than one pixel if the laser spot located at the boundary of a few pixels; the difference, however, may possibly stem from the measurement noise. In order to identify the actual size of the laser spot, we can increase the image resolution. However, this approach will reduce the speed of the camera due to the increase of sampling and recovery time. In next section, we

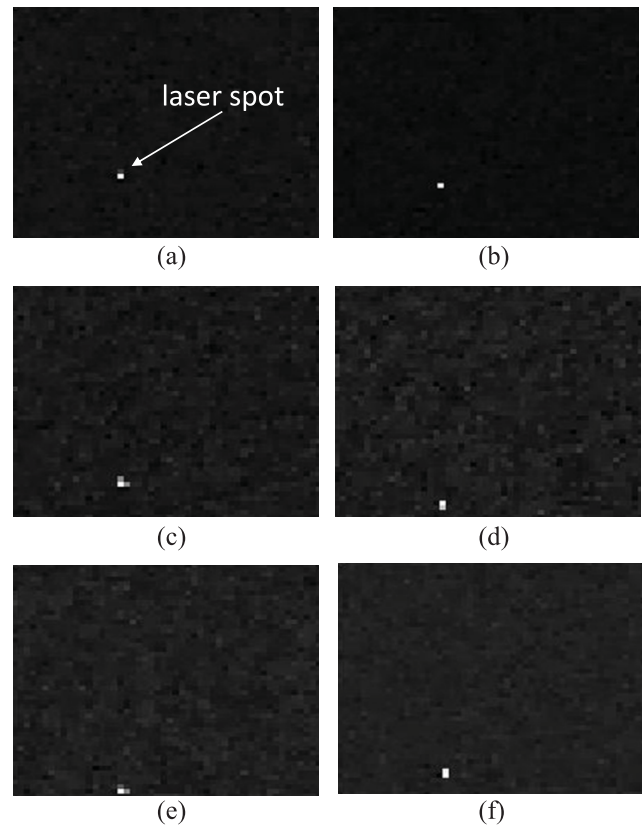


Fig. 8. Six images of a laser spot captured by our IR camera, showing the movement of the spot. (a) Infrared image shows the initial position of the laser spot. (b)–(e) Laser spot moved downward toward the bottom of the image. (f) Laser spot moved upward after it approached the bottom of the DMD.

will introduce the zooming technique to investigate the laser spot by keeping the same image resolution.

### D. Zooming

In previous experiments, all  $1024 \times 768$  micromirrors in the DMD were used to capture the IR images with a resolution of  $50 \times 50$  pixels. In such a setup, 315 micromirrors in unison represent one pixel, corresponding to an area of  $0.045 \text{ mm}^2$  on the DMD ( $144 \text{ } \mu\text{m}^2$  per micromirror). Therefore this camera setup is difficult to identify the features of an object with similar or smaller size than that area. We developed a zooming technique to investigate the details of small objects without degrading the performance of the camera.

The camera system can perform zooming in and out by varying the number of micromirrors for each pixel. When the camera worked in zooming-in mode, only a portion of the DMD was used as the measurement matrix generator. As a result, each pixel included fewer micromirrors. This mode is supported by the DMD because each individual micromirror can be controlled independently.

In order to verify the zooming concept, we designed an experiment to study the geometry and size of the IR laser spot shown in Fig. 8. In the zooming experiment, each IR image ( $50 \times 50$  pixels) was recovered using the same measurement matrix, number of measurements, and recovery algorithm as previous experiments. The only difference is the number of micromirrors for each pixel.

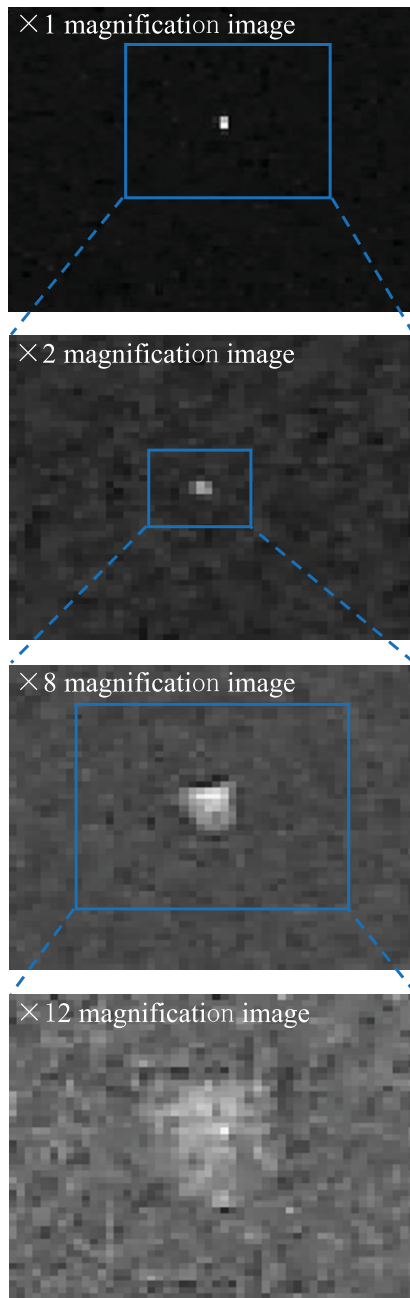


Fig. 9.  $\times 1$ ,  $\times 2$ ,  $\times 8$ , and  $\times 12$  magnification IR images captured by our IR camera. Their corresponding sections of DMD used to capture the images are highlighted by blue rectangles.

We first recovered an image ( $\times 1$  magnification image in Fig. 9) by using the whole DMD, which shows the laser spot covering two pixels, corresponding to  $0.090 \text{ mm}^2$  in area on the DMD. The intensity of each pixel for images in Fig. 9 is represented by 8 bits grey-scale: each pixel has a brightness from 0 to 255, where 0 is black and 255 is white. A typical OTSU method [55] is used to convert gray-scale images into binary images in order to identify the actual area of the laser spot. When we used  $521 \times 384$  micromirrors (highlighted by the blue rectangle in  $\times 1$  magnification image) to generate the measurement matrix, a  $\times 2$  magnification image was obtained. It is termed  $\times 2$  magnification because the micromirrors only cover half of the length and width of the DMD, while

the recovered image had same pixel number as the  $\times 1$  magnification image. The  $\times 2$  magnification image shows that a laser spot covered six pixels, reducing to  $0.068 \text{ mm}^2$  in area. We further sectioned the measurement matrix into  $130 \times 96$  micromirrors. The recovered  $\times 8$  magnification image shows that the laser spot covered forty one pixels, corresponding to  $0.029 \text{ mm}^2$  in area. A  $\times 12$  magnification image was obtained when we used  $85 \times 64$  micromirrors to generate the measurement matrix. A clear outline of the laser spot was exhibited in elliptical shape, which is similar to the laser spot geometry captured by a CMOS camera. The laser spot area was reduced to  $0.028 \text{ mm}^2$  in the  $\times 12$  magnification image. The experimental results showed that the shape and area of the laser spot are progressively refined to its actual geometry by zooming in with our camera system. It was also observed that images with larger magnification associated with lower image quality, since each pixel contained fewer micromirrors, which reflected less light to the photodetector.

This camera system is universal and adaptable. It is universal because we can use the same measurement matrix for all experiments [32]. The system is adaptable because the resolution of images and sections of DMD used for zooming can be adaptively adjusted depending on the features of objects.

## V. CONCLUSION

Nano-photodetectors have demonstrated promising performance to detect IR signals, especially CNT photodetectors. However, a small absorption area and the difficulties to fabricate a large scale photodetector array impede its application in imaging systems. In order to overcome these difficulties, a compressive sensing based IR camera system was developed. In the camera system, a single CNT field effect transistor integrated with a photonic cavity was employed to measure the compressed signals. Experimental results showed that the number of measurements required to recover the images can be much fewer than the pixel number of original images. This camera system was capable of observing the dynamic movement of a laser spot. A zooming technique was demonstrated to image the detailed structure of small features. This camera architecture provides a novel and alternative platform for future IR cameras, particularly the cameras using nano-photodetectors.

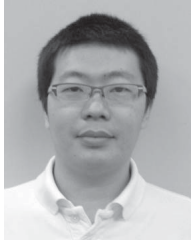
## REFERENCES

- [1] A. Rogalski, "Infrared detectors: An overview," *Infr. Phys. Technol.*, vol. 43, nos. 3–5, pp. 187–210, 2002.
- [2] F. Xia, T. Mueller, Y.-M. Lin, A. Valdes-Garcia, and P. Avouris, "Ultrafast graphene photodetector," *Nature Nanotechnol.*, vol. 4, no. 12, pp. 839–843, Dec. 2009.
- [3] K. W. Johnston, A. G. Pattantyus-Abraham, J. P. Clifford, S. H. Myrskog, D. D. MacNeil, L. Levina, and E. H. Sargent, "Schottky-quantum dot photovoltaics for efficient infrared power conversion," *Appl. Phys. Lett.*, vol. 92, no. 15, pp. 151115-1–151115-3, 2008.
- [4] B. F. Levine, "Quantum-well infrared photodetectors," *J. Appl. Phys.*, vol. 74, no. 8, pp. R1–R81, 1993.
- [5] C.-Y. Lu, S.-P. Chang, S.-J. Chang, C.-L. Hsu, Y.-Z. Chiou, and I.-C. Chen, "ZnO nanowire-based UV photodetector," *J. Nanosci. Nanotechnol.*, vol. 10, no. 2, pp. 1135–1138, 2010.



- [6] H. Chen, X. Sun, K. Lai, M. Meyyappan, and N. Xi, "Infrared detection using an InSb nanowire," in *Proc. IEEE Nanotechnol. Mater. Devices Conf.*, Jun. 2009, pp. 212–216.
- [7] X. Fang, S. Xiong, T. Zhai, Y. Bando, M. Liao, U. K. Gautam, Y. Koide, X. Zhang, Y. Qian, and D. Golberg, "High-performance blue/ultraviolet-light-sensitive ZnSe-nanobelt photodetectors," *Adv. Mater.*, vol. 21, no. 48, pp. 5016–5021, 2009.
- [8] H. Chen, N. Xi, K. Lai, C. Fung, and R. Yang, "CNT infrared detectors using Schottky barriers and p-n junctions based fets," in *Proc. Nanotechnol. Mater. Devices Conf.*, 2009, pp. 91–95.
- [9] P. Avouris, M. Freitag, and V. Perebeinos, "Carbon-nanotube photonics and optoelectronics," *Nature Photon.*, vol. 2, no. 6, pp. 341–350, 2008.
- [10] N. M. Gabor, Z. Zhong, K. Bosnick, J. Park, and P. L. McEuen, "Extremely efficient multiple electron-hole pair generation in carbon nanotube photodiodes," *Science*, vol. 325, no. 5946, pp. 1367–1371, 2009.
- [11] U. Bockelmann and G. Bastard, "Phonon scattering and energy relaxation in two-, one-, and zero-dimensional electron gases," *Phys. Rev. B*, vol. 42, no. 14, pp. 8947–8951, 1990.
- [12] C. A. Soci, A. A. Zhang, B. A. Xiang, S. A. A. Dayeh, D. P. R. A. Aplin, J. A. Park, X. Y. A. Bao, Y. H. A. Lo, and D. Y. Wang, "Zno nanowire UV photodetectors with high internal gain," *Nano Lett.*, vol. 7, no. 4, pp. 1003–1009, 2007.
- [13] P. G. Collins, M. S. Arnold, and P. Avouris, "Engineering carbon nanotubes and nanotube circuits using electrical breakdown," *Science*, vol. 292, no. 5517, pp. 706–709, 2001.
- [14] K. W. C. Lai, N. Xi, C. K. M. Fung, H. Chen, and T.-J. Tarn, "Engineering the band gap of carbon nanotube for infrared sensors," *Appl. Phys. Lett.*, vol. 95, no. 22, pp. 221107-1–221107-3, 2009.
- [15] M. B. Tzolov, T.-F. Kuo, D. A. Straus, A. Yin, and J. Xu, "Carbon nanotube silicon heterojunction arrays and infrared photocurrent responses," *J. Phys. Chem. C*, vol. 111, no. 15, pp. 5800–5804, 2007.
- [16] H. Chen, N. Xi, L. Chen, and K. Lai, "Carbon nanotube based multi-spectrum infrared detector array," in *Proc. 16th Int. Solid-State Sensors, Actuators, Microsyst. Conf.*, Jun. 2011, pp. 2566–2569.
- [17] Z. Fan, J. C. Ho, Z. A. Jacobson, H. Razavi, and A. Javey, "Large-scale, heterogeneous integration of nanowire arrays for image sensor circuitry," *Proc. Nat. Acad. Sci.*, vol. 105, no. 32, pp. 11066–11070, 2008.
- [18] I. A. Levitsky and W. B. Euler, "Photoconductivity of single-wall carbon nanotubes under continuous-wave near-infrared illumination," *Appl. Phys. Lett.*, vol. 83, no. 2, pp. 1857–1859, 2003.
- [19] J. Haupt and R. Nowak, "Compressive sampling vs. conventional imaging," in *Proc. Int. Conf. Image Process.*, Oct. 2006, pp. 1269–1272.
- [20] M. F. Duarte, M. A. Davenport, D. Takhar, J. N. Laska, T. Sun, K. F. Kelly, and R. G. Baraniuk, "Single-pixel imaging via compressive sampling," *IEEE Signal Process. Mag.*, vol. 25, no. 2, pp. 83–91, Mar. 2008.
- [21] H. Chen, N. Xi, B. Song, L. Chen, and K. Lai, "Single pixel infrared camera using a carbon nanotube photodetector," in *Proc. IEEE Sensors*, Oct. 2011, pp. 1362–1366.
- [22] M. A. Davenport, M. F. Duarte, Y. Eldar, and G. Kutyniok, *Introduction to Compressed Sensing*. Cambridge, U.K.: Cambridge Univ. Press, 2012, ch. 1.
- [23] M. Lustig, D. Donoho, and J. M. Pauly, "Sparse MRI: The application of compressed sensing for rapid MR imaging," *Magn. Reson. Med.*, vol. 58, no. 6, pp. 1182–1195, 2007.
- [24] J. Zhao, B. Song, N. Xi, K. W. C. Lai, H. Chen, and C. Qu, "Compressive feedback based non-vector space control," in *Proc. Amer. Control Conf.*, Jun. 2012, pp. 4090–4095.
- [25] B. Song, J. Zhao, N. Xi, K. W. C. Lai, R. Yang, H. Chen, and C. Qu, "Non-vector space control for nanomanipulations based on compressive feedbacks," in *Proc. IEEE Int. Conf. Robot. Autom.*, May 2012, pp. 2767–2772.
- [26] T. T. Y. Lin and F. J. Herrmann, "Compressed wavefield extrapolation," *Geophysics*, vol. 72, no. 5, pp. SM77–SM93, 2007.
- [27] S. Cotter and B. Rao, "Sparse channel estimation via matching pursuit with application to equalization," *IEEE Trans. Commun.*, vol. 50, no. 3, pp. 374–377, Mar. 2002.
- [28] E. Candès and M. Wakin, "An introduction to compressive sampling," *IEEE Signal Process. Mag.*, vol. 25, no. 2, pp. 21–30, Mar. 2008.
- [29] D. L. Donoho and M. Elad, "Optimally sparse representation in general (nonorthogonal) dictionaries via  $l_1$  minimization," *Proc. Nat. Acad. Sci.*, vol. 100, no. 5, pp. 2197–2202, 2003.
- [30] A. Cohen, W. Dahmen, and R. DeVore, "Compressed sensing and best  $k$ -term approximation," *J. Amer. Math. Soc.*, vol. 22, no. 1, pp. 211–231, 2009.
- [31] E. Candès, "The restricted isometry property and its implications for compressed sensing," *Comptes Rendus Math.*, vol. 346, nos. 9–10, pp. 589–592, 2008.
- [32] E. J. Candès and T. Tao, "Near optimal signal recovery from random projections: Universal encoding strategies?" *IEEE Trans. Inf. Theory*, vol. 52, no. 12, pp. 5406–5425, Dec. 2006.
- [33] E. Candès and T. Tao, "Decoding by linear programming," *IEEE Trans. Inf. Theory*, vol. 51, no. 12, pp. 4203–4215, Dec. 2005.
- [34] R. Baraniuk, M. Davenport, R. DeVore, and M. Wakin, "A simple proof of the restricted isometry property for random matrices," *Construct. Approx.*, vol. 28, no. 3, pp. 253–263, 2008.
- [35] J. A. Tropp and S. J. Wright, "Computational methods for sparse solution of linear inverse problems," *Proc. IEEE*, vol. 98, no. 6, pp. 948–958, Jun. 2010.
- [36] H. Chen, N. Xi, K. Lai, C. Fung, and R. Yang, "Development of infrared detectors using single carbon-nanotube-based field-effect transistors," *IEEE Trans. Nanotechnol.*, vol. 9, no. 5, pp. 582–589, Sep. 2010.
- [37] J. Zhang, N. Xi, K. W. C. Lai, H. Chen, Y. Luo, and G. Li, "Single carbon nanotube based photodiodes for infrared detection," in *Proc. 7th IEEE Int. Conf. Nanotechnol.*, Hong Kong, Aug. 2007, pp. 1156–1160.
- [38] K. W. C. Lai, N. Xi, C. K. M. Fung, J. Zhang, H. Chen, Y. Luo, and U. C. Wejinya, "Automated nanomanufacturing system to assemble carbon nanotube based devices," *Int. J. Robot. Res.*, vol. 28, no. 4, pp. 523–536, 2009.
- [39] J. Zhang, N. Xi, L. Liu, H. Chen, K. Lai, and G. Li, "Atomic force yields a master nanomanipulator," *IEEE Nanotechnol. Mag.*, vol. 2, no. 2, pp. 13–17, Jun. 2008.
- [40] J. Zhang, N. Xi, H. Chen, K. W. C. Lai, G. Li, and U. Wejinya, "Photovoltaic effect in single carbon nanotube-based Schottky diodes," *Int. J. Nanoparticles*, vol. 1, no. 2, pp. 108–118, 2008.
- [41] H. Z. Chen, N. Xi, K. W. C. Lai, L. L. Chen, R. G. Yang, and B. Song, "Gate dependent photo-responses of carbon nanotube field effect phototransistors," *Nanotechnology*, vol. 23, no. 38, p. 385203, 2012.
- [42] H. Chen, N. Xi, K. Lai, L. Chen, C. Fung, and J. Lou, "Plasmonic-resonant bowtie antenna for carbon nanotube photodetectors," *Int. J. Opt.*, vol. 2012, pp. 318104-1–318104-9, Mar. 2012.
- [43] C. K. M. Fung, N. Xi, B. Shanker, and K. W. C. Lai, "Nanoresonant signal boosters for carbon nanotube based infrared detectors," *Nanotechnology*, vol. 20, no. 18, pp. 185201-1–185201-6, 2009.
- [44] Y. Akahane, T. Asano, B. Song, and S. Noda, "High-Q photonic nanocavity in a two-dimensional photonic crystal," *Nature*, vol. 425, no. 6961, pp. 944–947, 2003.
- [45] M. Bayindir and E. Ozbay, "Heavy photons at coupled-cavity waveguide band edges in a three-dimensional photonic crystal," *Phys. Rev. B*, vol. 62, no. 4, pp. R2247–R2250, 2000.
- [46] S. Noda, K. Tomoda, N. Yamamoto, and A. Chutinan, "Full three-dimensional photonic bandgap crystals at near-infrared wavelengths," *Science*, vol. 289, no. 5479, pp. 604–606, 2000.
- [47] T. Baba, D. Sano, K. Nozaki, K. Inoshita, Y. Kuroki, and F. Koyama, "Observation of fast spontaneous emission decay in GaInAsP photonic crystal point defect nanocavity at room temperature," *Appl. Phys. Lett.*, vol. 85, no. 18, pp. 3989–3991, 2004.
- [48] H. Chen, N. Xi, J. Lou, K. Lai, L. Chen, and B. Song, "Photonic crystal with a HfO<sub>2</sub> defect to improve performance of carbon nanotube based photodetectors," in *Proc. 11th IEEE Conf. Nanotechnol.*, Aug. 2011, pp. 978–981.
- [49] M. Jerman, Z. Qiao, and D. Mergel, "Refractive index of thin films of SiO<sub>2</sub>, ZrO<sub>2</sub>, and HfO<sub>2</sub> as a function of the films' mass density," *Appl. Opt.*, vol. 44, no. 15, pp. 3006–3012, 2005.
- [50] H. W. Hubers, J. Schubert, A. Krabbe, M. Birk, G. Wagner, A. Semenov, and G. Goltsman, "Parylene anti-reflection coating of a quasi-optical hot-electron-bolometric mixer at terahertz frequencies," *Infr. Phys. Technol.*, vol. 42, no. 1, pp. 41–47, 2001.
- [51] L. Chen, N. Xi, H. Chen, and K. Lai, "Development of readout system for carbon nanotube based infrared detector," in *Proc. Nanotechnol. Mater. Devices Conf.*, 2010, pp. 230–234.
- [52] L. Chen, N. Xi, H. Chen, and K. W. C. Lai, "High gain current readout method for MWCNT infrared sensor," in *Proc. 12th IEEE Conf. Nanotechnol.*, Mar. 2012, pp. 1–4.

- [53] J. Appenzeller, M. Radosavljević, J. Knoch, and P. Avouris, "Tunneling versus thermionic emission in one-dimensional semiconductors," *Phys. Rev. Lett.*, vol. 92, no. 4, pp. 048301-1-048301-4, 2004.
- [54] J. Zhang, N. Xi, H. Chen, K. Lai, G. Li, and U. Wejinya, "Design, manufacturing, and testing of single-carbon-nanotube-based infrared sensors," *IEEE Trans. Nanotechnol.*, vol. 8, no. 2, pp. 245-251, Mar. 2009.
- [55] N. Otsu, "A threshold selection method from gray-level histograms," *IEEE Trans. Syst. Man Cybern.*, vol. 9, no. 1, pp. 62-66, Jan. 1979.



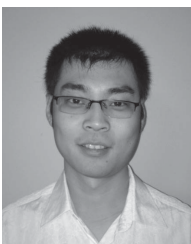
**Hongzhi Chen** (S'06) received the B.Eng. degree in information engineering from the Guangdong University of Technology, Guangzhou, China, in 2005, and the M.Sc. degree in electronics from Queen's University Belfast, Belfast, U.K., in 2006. He is currently pursuing the Ph.D. degree with the Department of Electrical and Computer Engineering, Michigan State University, East Lansing.

His current research interests include nano-electronics, nano-photonics, sensors, micro/nanofabrication and manufacturing, scanning probe microscopy, device characterization, MEMS/NEMS, and micro/nanorobotics and systems.



**Ning Xi** (S'89-M'92-SM'05-F'07) received the D.Sc. degree in systems science and mathematics from Washington University, St. Louis, Missouri, in 1993, and the B.S. degree in electrical engineering from the Beijing University of Aeronautics and Astronautics, Beijing, China.

He is the University Distinguished Professor and John D. Ryder Professor of electrical and computer engineering with Michigan State University, East Lansing. His current research interests include robotics, manufacturing automation, micro/nano manufacturing, nano sensors and devices, and intelligent control and systems.



**Bo Song** (S'08) received the B.Eng. degree in mechanical engineering from the Dalian University of Technology, Dalian, China, in 2005, and the M.Eng. degree in electrical engineering from the University of Science and Technology of China, Hefei, China, in 2009. He is currently pursuing the Ph.D. degree with the Department of Electrical and Computer Engineering, Michigan State University, East Lansing.

His current research interests include nanorobotics, nonvector space control, compressive sensing, and biomechanics.



**Liangliang Chen** was born in Jiangsu, China, in 1985. He received the Bachelors and Masters degree in electrical engineering from the Huazhong University of Science and Technology, Wuhan, China, in 2009 and 2007, respectively. He is currently pursuing the Ph.D. degree with Michigan State University, East Lansing.

His current research interests include ultra weak signal detection in nano sensors, signal processing, analog circuits, and CNT nano sensors.



**Jianguo Zhao** (S'06) received the B.E. degree in mechanical engineering from the Harbin Institute of Technology, Harbin, China, in 2005, and the M.E. degree in mechatronic engineering from Shenzhen Graduate School, Harbin Institute of Technology, Shenzhen, China, in 2007. He is currently pursuing the Ph.D. degree with the Robotics and Automation Laboratory, Michigan State University, East Lansing.

His current research interests include biologically inspired robotics, dynamics and control, visual servoing, and mobile sensor network.



**King Wai Chiu Lai** (M'05) received the Ph.D. degree from the Department of Automation and Computer-Aided Engineering, Chinese University of Hong Kong, Hong Kong, in 2005.

He has been a Post-Doctoral Research Associate and the Lab Manager with the Department of Electrical and Computer Engineering, Michigan State University, East Lansing, since 2006. Currently, he is an Assistant Professor with the Department of Mechanical and Biomedical Engineering, City University of Hong Kong. He has authored or co-authored more than 80 high-quality journals, book chapters, and conference papers. His current research interests include investigation of atomic force microscope-based nano-manufacturing technology and the development of nano optoelectronic sensors and devices.



**Ruiguo Yang** (S'08) received the B.Eng. degree in mechanical engineering and the M.Eng. degree in mechanical and electrical engineering from the Nanjing University of Aeronautics and Astronautics, Nanjing, China, in 2004 and 2007, respectively. He is currently pursuing the Ph.D. degree with the Department of Electrical and Computer Engineering, Michigan State University, East Lansing.

His current research interests include micro/nano-robotics and systems, micro/nanomanufacturing, nanomechanics, biomechanics, bioMEMS and biomedical imaging, and characterization and modeling.